A&A, 714, A420 (2026)
https://doi.org/10.1051/0004-6361/202660065
© The Authors 2026

Astronomy & Astrophysics

SDSS-V BHM: Evidence for a link between X-ray weakness and galaxy-scale ionised gas outflows in quasars

Delvin Demke[1,⋆], Dominika Wylezalek[1], Daniel R. Wik[1,2], M. Vivek[1,3], Amy L. Rankine[4], W. N. Brandt[5,6,7], Donald P. Schneider[5,6], Roberto J. Assef[8], Catarina Aydar[9,10], and Scott F. Anderson[11]

[1] Zentrum für Astronomie der Universität Heidelberg Astronomisches Rechen-Institut Mönchhofstr 12–14, 69120 Heidelberg, Germany
[2] University of Utah Department of Physics and Astronomy, Salt Lake City, UT, USA
[3] Indian Institute of Astrophysics, Koramangala II block, Bangalore 560034, Karnataka, India
[4] Institute for Astronomy, University of Edinburgh, Royal Observatory, Blackford Hill, Edinburgh EH9 3HJ, UK
[5] Department of Astronomy and Astrophysics, 525 Davey Lab, The Pennsylvania State University, University Park, PA 16802, USA
[6] Institute for Gravitation and the Cosmos, The Pennsylvania State University, University Park, PA 16802, USA
[7] Department of Physics, 104 Davey Laboratory, The Pennsylvania State University, University Park, PA 16802, USA
[8] Instituto de Estudios Astrofísicos, Facultad de Ingeniería y Ciencias, Universidad Diego Portales, Av. Ejército Libertador 441, Santiago, Chile
[9] Max Planck Institute for Extraterrestrial Physics, Gießenbachstraße 1, 85748 Garching, Germany
[10] Excellence Cluster ORIGINS, Boltzmannstrasse 2, 85748 Garching, Germany
[11] Department of Astronomy, University of Washington, Box 351580, Seattle, WA 98195, USA

Received 25 March 2026 / Accepted 8 September 2026

ABSTRACT

Active galactic nuclei (AGNs) are among the most powerful engines in the Universe. A central open question is how accretion physics, obscuration, and feedback are intertwined in shaping these systems. This paper presents an analysis of SDSS-V–eROSITA Data Level 1 (DL1) data from the 19th data release (DR19). The work is based on SDSS spectra for 2119 soft X-ray selected quasars ($0 < z < 0.95$), drawn from the eROSITA all-sky catalogue (eRASS1), and complemented by mid-infrared (MIR) data from the Wide-field Infrared Survey Explorer (WISE). We assessed the outflow strength using the W_{80} measurement of the [O III] λ5007 emission line and derived the virial black hole mass from the broad $H\beta$ emission line. The rest-frame 2–10 keV X-ray luminosity and the 6 µm MIR luminosity were used to determine the X-ray weakness, relative to established luminosity scaling relations. We compared the W_{80}line width, X-ray luminosity, and black hole mass and report a weak negative trend between X-ray weakness and outflow strength for quasars with $W_{80} \geq 800\,\mathrm{km\,s^{-1}}$. These results support the interpretation that the observed X-ray weakness in AGNs may be linked to dense, nuclear-scale outflows.

Key words. galaxies: active – galaxies: general – quasars: general – quasars: supermassive black holes – X-rays: galaxies

1. Introduction

One of the most luminous classes of extragalactic objects is quasars, active galactic nuclei (AGNs) powered by rapidly accreting supermassive black holes (SMBHs) with bolometric luminosities exceeding $L_{bol} \gtrsim 10^{45}$ erg s^{-1} (e.g. Alexander & Hickox 2012). During this phase of rapid SMBH growth, quasars release enormous amounts of radiative and mechanical energy. Observations across the electromagnetic spectrum increasingly support a picture in which luminous quasars undergo an evolutionary 'blowout' phase, during which efficient accretion triggers powerful outflows that begin to clear gas and dust from the central regions. Such a phase is predicted by co-evolutionary models linking SMBH growth and galaxy evolution and is thought to play a key role in regulating star formation and influencing the interstellar and circumgalactic medium (e.g. Silk & Rees 1998; Fabian 1999; Benson et al. 2003; King 2003; Hopkins et al. 2006, 2008; Harrison et al. 2014). Observationally, the energetics of molecular and ionised outflows are found to scale with bolometric luminosity (Fiore et al. 2017), implying that quasar-driven feedback becomes increasingly important at high accretion rates.

The cosmic star formation rate density and the SMBH accretion rate density both peak at $z \sim 2$–3, suggesting a close connection between galaxy growth and black hole accretion over cosmic time (e.g. Madau & Dickinson 2014). While this cosmic co-evolution describes global trends, individual quasars are also thought to pass through different evolutionary stages. Dust-obscured galaxies (DOGs), characterised by extremely high infrared luminosities, are commonly interpreted as systems in which the central engine is heavily buried (e.g. Narayanan et al. 2010). Similar objects are hot DOGs (e.g. Eisenhardt et al. 2012), extremely red quasars (ERQs; e.g. Hamann et al. 2017), and heavily reddened type 1 quasars (e.g. Banerji et al. 2015). These obscured quasar populations provide key laboratories for testing how galaxy-scale obscuration and inner accretion physics manifest in the observed emission. In particular, it is important to distinguish between evolutionary interpretations, in which obscured systems represent a phase in the quasar

⋆ Corresponding author: d.demke01@gmail.com

Open Access article, published by EDP Sciences, under the terms of the Creative Commons Attribution License (https://creativecommons.org/licenses/by/4.0), which permits unrestricted use, distribution, and reproduction in any medium, provided the original work is properly cited.
This article is published in open access under the Subscribe to Open model. Subscribe to A&A to support open access publication.

lifecycle, and physical mechanisms responsible for their high-energy emission properties. While DOGs, hot DOGs, and ERQs are often interpreted within an evolutionary framework in which quasars transition from a heavily obscured to unobscured phase (Hopkins et al. 2006), the physical origin of their observed X-ray weakness remains debated. In particular, it is unclear whether the X-ray deficit primarily reflects galaxy-scale obscuration associated with evolutionary stages or whether it arises from processes intrinsic to the central engine, such as suppression of the X-ray corona or shielding gas linked to accretion-disk winds (Brandt & Alexander 2015; Hickox & Alexander 2018).

The key diagnostic for probing the physical state of accreting AGNs and identifying deviations caused by obscuration is the relationship between the mid-infrared (MIR) dust continuum luminosity and X-ray luminosity. Mid-infrared emission, emitted by AGNs, traces reprocessed radiation from the dusty torus, while hard X-rays originate in the hot corona close to the accretion disk and trace the emission from the innermost accretion flow. A tight correlation between these quantities has been established for nearby, predominantly unobscured AGNs, in particular local Seyfert galaxies, and has been shown to extend to luminous quasars (Lutz et al. 2004; Gandhi et al. 2009; Stern 2015). While most quasars follow this correlation, a subset appears significantly underluminous in the X-ray relative to their MIR emission. Such objects are commonly referred to as 'X-ray weak' quasars (Brandt et al. 2000; Gibson et al. 2009).

The term 'X-ray weakness' encompasses a range of observational phenomena and does not necessarily imply a single physical origin. For highly accreting quasars, larger bolometric corrections can result in an apparent X-ray weakness when compared at fixed bolometric luminosities, although these sources may still possess high absolute X-ray luminosities (Lusso et al. 2012; Duras et al. 2020). Such sources can nevertheless exhibit high absolute X-ray luminosities and do not necessarily require strong obscuration or suppressed coronal emission. At very high redshifts ($z > 5$), quasars with steep X-ray spectra ($\Gamma > 2$) may also appear X-ray weak because their emission is shifted towards energies where current X-ray observatories have reduced sensitivity (Zappacosta et al. 2023; Tortosa et al. 2024). These examples demonstrate that the physical interpretation of X-ray weakness depends on the properties of the population studied.

For the observed MIR-normalised X-ray deficits considered in this work, several physical mechanisms have been proposed. These include heavy absorption, intrinsically weak coronal emission, or a combination of both effects (e.g. Leighly et al. 2007; Luo et al. 2013; Pu et al. 2020). Changes in the structure of the inner accretion flow may also modify the relative contribution of the X-ray emitting corona. For example, in warm corona scenarios, a significant fraction of the accretion power is dissipated in an optically thick, warm Comptonising medium, altering the hard X-ray emission component (e.g. Petrucci et al. 2018). Obscuration is frequently observed in some rapidly growing quasar populations (Menci et al. 2008; Assef et al. 2015), and studies of DOGs and MIR-luminous AGNs have found column densities frequently approaching Compton-thick regimes (Ricci et al. 2015; Goulding et al. 2018; Ishikawa et al. 2021; Yu et al. 2024). For many such systems, correcting for absorption restores agreement with established MIR-X-ray relations, indicating that obscuration can dominate the observed X-ray deficit (Wang et al. 2022). However, some objects remain X-ray weak after accounting for absorption, suggesting that intrinsic suppression of the corona may also contribute (Luo et al. 2013). Recent NuSTAR observations further suggest that several candidates previously interpreted as intrinsically X-ray weak can instead be explained by complex obscuration, leaving the relative importance of intrinsic coronal suppression uncertain (Wang et al. 2022).

A physically motivated framework linking observed X-ray deficits and accretion-disk winds is provided by the shielding-gas scenario, in which a layer of highly ionised gas located in the ultraviolet (UV) line-driven wind absorbs a substantial fraction of the X-ray and extreme ultraviolet (EUV) emission produced near the corona (Murray et al. 1995; Proga et al. 2000). By suppressing the ionising continuum, this shielding gas prevents material at large radii from becoming overionised, thereby enabling efficient radiative acceleration via line driving (Proga et al. 2000). This mechanism naturally leads to faster and stronger winds while simultaneously producing an apparent X-ray deficit. Observational support for this picture comes from broad absorption line (BAL) quasars, which host sub-parsec scale winds reaching velocities of several thousand kilometres per second. While many BAL quasars have historically been found to exhibit suppressed X-ray emission relative to their UV luminosities (Weymann et al. 1991; Brandt et al. 2000; Laor & Brandt 2002; Gibson et al. 2009), more recent analyses using the Sloan Digital Sky Survey (SDSS) Data Release 19 (DR19) and eROSITA data suggest that BAL and non-BAL quasars can exhibit comparable X-ray emission relative to their optical/UV luminosities (e.g. Hiremath et al. 2025). However, this result may partly reflect differences in sample selection, since X-ray-selected samples naturally favour X-ray-bright sources. In some models, the shielding gas arises from a 'failed wind' that does not reach escape velocities owing to overionisation (Proga & Kallman 2004; Sim et al. 2010). However, the necessity of such a configuration has been questioned, since radiation pressure confinement models can account for the observed ionisation structure and column densities of BAL outflows without requiring a distinct failed-wind shielding layer (Baskin et al. 2014).

While BAL winds trace outflows close to the accretion disk, the impact of AGN-driven winds on larger scales is commonly probed using the kinematics of the [O III] λ5007 emission line, which traces ionised gas in the narrow-line region on kiloparsec scales (Harrison et al. 2018). Broad and blueshifted [O III] lines provide a sensitive measure of large-scale outflow strengths. Small samples and individual extreme objects have shown a link between high [O III] velocities and heavy obscuration in X-rays, including cases consistent with Compton-thick absorption (Goulding et al. 2018; Ishikawa et al. 2021). However, previous studies have lacked the large, homogeneous, multi-wavelength datasets required for the statistical testing of the relationship between observed X-ray weakness and outflow strength across a representative quasar population.

The advent of the first eROSITA all-sky catalogue (eRASS1; Merloni et al. 2024) provides a unique opportunity to address this question. As part of the fifth generation of the Sloan Digital Sky Survey (SDSS-V; Kollmeier et al. 2026), eRASS1 X-ray detections have been observed with SDSS-V spectroscopy, enabling the construction of a large, uniform sample of quasars with consistent optical and X-ray luminosities. In this work, we define X-ray weakness as an observed deficit in rest-frame 2–10 keV luminosity relative to the expectation from established MIR–X-ray correlations. We exploited this dataset to investigate the statistical connection between such MIR-normalised X-ray deficits and galaxy-scale outflow strength for 2119 quasars at $0 < z < 0.95$. This approach allows us to characterise the connection between coronal emission, obscuration, and outflows across a broad range of luminosities and physical conditions and to

identify promising targets for future spatially resolved outflow studies and deep X-ray observations.

The paper is organised as follows. We introduce the data in Sect. 2, followed by the analysis methodology and sample selection in Sect. 3. The results are presented in Sect. 4, and our conclusion is summarised in Sect. 5. Throughout this work, we assume a flat cosmology with $h = 0.7$, $\Omega_M = 0.3$, and $\Omega_\Lambda = 0.7$.

2. Data

The data for this investigation are provided by a collaboration between the Spectrum-Roentgen Gamma (SRG)/eROSITA X-ray telescope (Predehl et al. 2021) and SDSS. The X-ray data are based on a sample of X-ray detected sources from eRASS1 data (Merloni et al. 2024), covering half of the sky in the 0.2–2.3 keV band. With a sensitivity of 10^{-14}–10^{-13} erg cm^{-2} s^{-1} in the 0.2–2.3 keV band, eRASS1 can detect previously unknown X-ray sources. Assuming a photon index of $\Gamma = 1.8$, this corresponds to a median 2–10 keV luminosity limit of $L_X > 10^{41}$ erg s^{-1} at $z = 0.05$, and $L_X > 10^{44}$ erg s^{-1} at $z = 1$. The available spectra were obtained as part of the spectroscopic identification of eROSITA sources (SPIDERS; Dwelly et al. 2017; Comparat et al. 2020; Aydar et al. 2025) survey, which was created during SDSS-IV and continued as one of the projects of SDSS-V within the Black Hole Mapper (BHM, Kollmeier et al. 2026). The spectra cover a wavelength range between 3600 Å to 10 400 Å (Bowen & Vaughan 1973; Gunn et al. 2006; Smee et al. 2013), with a resolution of $R = 1560$–2650.

The SPIDERS Data Level 1 (DL1) catalogue used in this work includes 9753 quasars at $0 < z < 5.23$ (Sect. 7.2, SDSS Collaboration 2026). The catalogue includes X-ray to optical and infrared cross-matching, which was performed by Salvato et al. (2022, 2025) and additionally includes cross-matches with several surveys. The MIR photometry was extracted from the Wide-field Infrared Survey Explorer (WISE; Wright et al. 2010). The catalogue used is `catWISE2020` (Marocco et al. 2021). The SDSS-V pipeline (Bolton et al. 2012) provides a spectroscopic classification and redshift estimate for each target. We restricted our sample to sources classified as quasars (`QSO`). To ensure a minimum spectral quality for reliable redshift determination and subsequent emission-line measurements, we additionally required a median signal-to-noise ratio (S/N) for the full spectra of `sdss_sn_median_all` > 2. We further selected quasars with unflagged spectroscopic redshifts (`sdss_zwarning` = 0) and limited the sample to $z \leq 1$ (top panel Fig. 1), ensuring that both the Hβ and [O III] emission lines are covered by the observed spectral range.

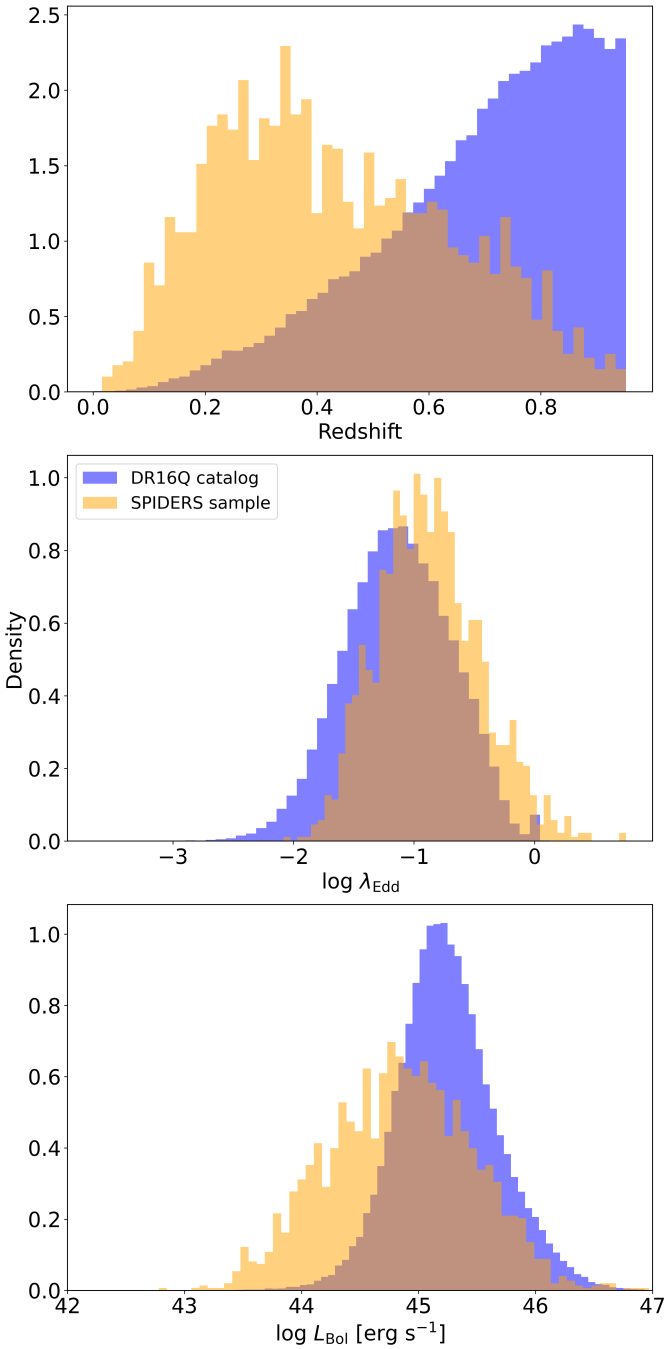


Fig. 1. Comparison of the normalised distributions of the SPIDERS AGN and the SDSS DR16 quasar catalogues (Wu & Shen 2022). Shown are redshift (top), Eddington ratio (middle), and bolometric luminosity (bottom).

3. Spectral analysis and sample selection

This section describes the analysis of the optical SDSS-V spectra (Sect. 3.1). We then detail how we derived the MIR and X-ray luminosities (Sect. 3.2), including the explicit definition and implementation of our X-ray weakness metric ΔL_X (Sect. 3.2.3). Example spectra covering the parameter space are presented in Appendix D.

3.1. SDSS data

3.1.1. Continuum and emission-line fitting

The optical spectra analysed here were drawn from SDSS-V DR19 (SDSS Collaboration 2026). All spectra were corrected for Galactic extinction using the Fitzpatrick (1999) reddening law and converted to the rest frame using the pipeline redshifts. We modelled the continuum and emission-line regions using the Bayesian AGN decomposition for SDSS spectra tool (`BADASS3`, Sexton et al. 2021)[1]. The continuum model comprises (i) a power-law AGN continuum (Calderone et al. 2017), (ii) an optical FeII emission template (broad and narrow) from Véron-Cetty et al. (2004), and (iii) a host-galaxy single stellar population model from the MILES Tune Stellar Libraries Webtool (Vazdekis et al. 2010), with ages of 0.1, 0.5, 1.0, 2.0,

[1] GitHub: `BADASS3`

5.0, 10.0, and 13.0 Gyr and metallicities in the standard approach by BADASS3. Fitting was performed over the rest-frame wavelength range [4400–5500] Å.

Emission line profiles were modelled using Gaussian functions for both the narrow and broad components. For the narrow lines, the velocity dispersion was constrained to the range [0–1000] km s^{-1}, while for the broad lines it was allowed to vary between [300-3000] km s^{-1}. The velocity offset was limited between [-500, +500] km s^{-1} for the narrow components and [–1000, +1000] km s^{-1} for the broad components. These limits were chosen to ensure physically plausible fits and to avoid degeneracies between neighbouring features.

To estimate parameter uncertainties, we ran a Markov chain Monte Carlo sampler (implemented in `BADASS3`; Sexton et al. 2021). For computational efficiency, given the more than 6000 spectra, we used a maximum of 1500 steps with a 1000-step burn-in. We fitted Hβ at rest-frame wavelength 4862.691 Å and the [O III] $\lambda\lambda$ 4959, 5007 Å doublet. The broad Hβ component and the [O III] λ5007 Å model parameters were largely allowed to vary freely. The velocity dispersion and the velocity offset of the [O III] doublet were tied together, and the flux ratio was fixed at 1:2.98 based on the atomic parameters of Dimitrijević et al. (2007). The velocity dispersion of the narrow Hβ components was tied to that of the narrow [O III] λ5007 Å component.

Every spectrum was fitted twice: once with a single narrow Gaussian component for [O III] λ5007 Å, and once with two narrow Gaussian components. The preferred model was selected according to the following criteria: an overall fit quality of $R^2 > 0.8$, where R^2 denotes the coefficient of determination (i.e. the fraction of variance explained by the model), a (S/N) > 7 for the first component, and (S/N) > 3 for the second component. Among fits satisfying these criteria, the model with reduced χ^2 closest to one was chosen (Albán et al. 2024). For each spectrum, `BADASS3` provides the best-fit value and uncertainties for amplitude, dispersion, equivalent width, flux, full width at half maximum (FWHM), luminosity, S/N, velocity offset, and W_{80} (Sect. 3.1.2) for every line component. It additionally returns combined measurements for blended complexes (suffix `_COMB`). Velocity-space parameters (FWHM and W_{80}) are corrected for the wavelength-dependent instrumental resolution of the SDSS spectrograph, indicated by the suffix `_COR`.

For sources with multiple spectroscopic observations, we retained one epoch per object to represent the spectral measurements and derived parameters. For each epoch, we computed the inverse-variance (IV) sum of the key fit uncertainties ($1/\sigma^2$ for `mass_bh`, and `w80`), the global spectrum median S/N (`sdss_sn_median_all`), and the S/N of the primary and, when available, the secondary [O III] component. We compared epochs using their respective preferred models, without imposing a fixed single- or double-Gaussian parametrisation across observations. When the selected epoch differed in model complexity from other available epochs, we visually verified that the adopted solution provided the most reliable representation of the line profile. Each metric was normalised across the epochs of the same object and combined as a figure-of-merit

$$\begin{aligned}\mathrm{FoM} = {} & \omega_{\mathrm{IV}}\,\mathrm{IV}_{\mathrm{norm}} + \omega_{\mathrm{SN}}\,\mathrm{SN}_{\mathrm{norm}} \\ & + \omega_{[\mathrm{O\,III}]}\left(\mathrm{SN}_{[\mathrm{O\,III}],\mathrm{norm}} + \mathrm{SN}_{[\mathrm{O\,III}],2,\mathrm{norm}}\right), \end{aligned} \quad (1)$$

and we selected the epoch with the highest FoM as the representative spectrum for this quasar. We tested the robustness of the FoM epoch selection against 216 combinations of weights (ω) assigned to the IV term (ω_{IV} = 0.40–0.80) and to the global spectral S/N (ω_{SN} = 0.15–0.45). The remaining weight, constrained to ≤0.2, was attributed to the [O III] S/N, either entirely to the primary component or equally split between primary and secondary components. We found that the epoch ranking is stable across a broad region of parameter space, with only minor changes in sample membership, i.e. only a small fraction of objects had a different epoch selected under alternative weighting schemes, and no statistically significant differences in the derived parameter distributions. We therefore adopted the baseline configuration $\omega_{IV} = 0.6$, $\omega_{SN} = 0.4$, and $\omega_{OIII} = 0.05$.

We additionally compared our fitting results with the SDSS DR19 quasar spectral property catalogue (qVAC; Wu & Shen 2022). This catalogue focuses on quasars with little to no visible host contamination. A comparison of the qVAC and the `BADASS3` results reveals differences in certain parameters. The qVAC fitting procedure restricted their narrow components to a velocity dispersion <600 km s^{-1}, which resulted in a plateau and an underestimation of the measured [O III] width. Furthermore, the qVAC estimated masses are higher than our black hole masses (more details in Appendix C). After an exchange with the creators of the catalogue, we decided not to use the qVAC results. For sources at $z < 1$, a dedicated host-decomposition is required because stellar emission from the host galaxy can contribute significantly to the observed optical continuum, leading to overestimates of the AGN luminosity. This decomposition is not included in the version of the qVAC used here. Moreover, a potential underestimation of the [O III] line width could bias interpretations of the relation between X-ray weakness and strong ionised outflows.

3.1.2. [O III] kinematics

We characterised the ionised gas kinematics using the [O III] λ5007 Å emission line. As a non-parametric velocity-width measure, we adopted $W_{80} = \mathrm{v}_{90} - \mathrm{v}_{10}$, where v_{90} and v_{10} denote the velocities at which 90% and 10% of the cumulative line flux are reached, respectively, such that W_{80} encloses 80% of the total line flux (Liu et al. 2013). This measure is less sensitive to asymmetric wings than a Gaussian FWHM and better captures broad components associated with outflows. `BADASS3` provides W_{80} values for both single Gaussian and double Gaussian emission fits, based on the models. Following the literature (Harrison et al. 2014), we separated the quasars into sources with significant outflow signatures ($W_{80} \geq 800$ km s^{-1}) and those with narrow or non-prominent outflows.

3.1.3. Black hole masses, bolometric luminosities, and Eddington ratios

Black hole masses were estimated using the single-epoch virial method, which relates the broad-line region (BLR) kinematics and the continuum luminosity to the virial mass (Greene & Ho 2005; Vestergaard & Peterson 2006; Shen 2013). For the redshift range of our sample, the $H\beta$ line is covered by the SDSS spectra. From the `BADASS3` fits, we extracted the FWHM of the broad $H\beta$ component and the monochromatic continuum luminosity at 5100 Å, λL_λ. We adopted the calibration of Shen et al. (2011):

$$\log\left(\frac{M_{\mathrm{BH}}}{M_\odot}\right) = a + 2\log\left(\frac{\mathrm{FWHM}}{\mathrm{km\,s^{-1}}}\right) + b\log\left(\frac{\lambda \mathrm{L}_\lambda}{10^{44}\,\mathrm{erg\,s^{-1}}}\right), \quad (2)$$

with $(a, b) = (0.91, 0.5)$ (Vestergaard & Peterson 2006). The estimated uncertainty is purely statistical and does not include the systematic uncertainty of approximately 0.4 dex (Shen 2013). An

additional source of uncertainty arises from the blending of the [O III] doublet with the red wing of Hβ. This effect is negligible when $H\beta$ and [O III] are fitted simultaneously (Bertemes et al. 2025).

The derived masses span $5.63 < \log(M_{\rm BH}/M_\odot) < 9.51$, with a mean value of $\log(M_{\rm BH}/M_\odot) = 7.55$. We achieved a completeness of 81% when requiring an error-to-value ratio of <0.2, which selects sources with a reliably detected broad $H\beta$ component. Objects with large error ratios (especially >1) show weak or poorly constrained broad $H\beta$ emission. Although the SDSS pipeline classifies these sources as QSO, implying the presence of broad emission lines, a subset of objects in our sample shows $H\beta$ profiles without a clearly significant broad component. One possible explanation is that the broad wings are hidden below the noise level, as many of these sources lie close to the adopted lower S/N threshold. In some cases, the broad $H\beta$ component may also be intrinsically narrow, corresponding to quasars with relatively low broad-line widths. In addition, partial obscuration of the BLR could further reduce the observed strength of the broad component, making it more difficult to detect and constrain reliably.

To characterise the sample in terms of accretion properties, we computed the bolometric luminosity and the Eddington ratios for all sources. The bolometric luminosity was estimated following Runnoe et al. (2012) as

$$\log L_{bol} = 4.891 + 0.912 \log\ L5100, \tag{3}$$

where $L5100$ is the monochromatic luminosity at 5100 Å, expressed in units of erg s^{-1}. Together with the virial black hole mass estimates, these values were used to derive the Eddington ratio,

$$\log \lambda_{\rm Edd} = \log L_{bol} - \log\left(1.26 \times 10^{38}\right) - \log\left(\frac{M_{\rm BH}}{M_\odot}\right). \tag{4}$$

A comparison with the SDSS DR16 quasar catalogue (Wu & Shen 2022) shows that we have more nearby sources, whereas the quasar catalogue extends to higher redshifts. The SPIDERS sample exhibits slightly lower bolometric luminosities but systematically higher Eddington ratios (Fig. 1). This likely reflects the X-ray-based target selection of SPIDERS, which preferentially identifies nearby AGNs over a broad range of obscuration and luminosity. Compared with optically selected quasar samples, this difference in selection function can naturally lead to different observed distributions of Eddington ratios (Brandt & Alexander 2015; Hickox & Alexander 2018). After applying our criteria on S/N, X-ray detection likelihood, and sufficient [O III] detection, our final working sample consists of 2119 quasars at $0 < z < 0.95$.

3.2. X-ray and MIR properties

To compare the available MIR and X-ray emission, we converted observed fluxes into rest-frame luminosities. The MIR monochromatic luminosity ($\nu L\nu(6\,\mu\text{m})$) traces thermal re-emission from the dusty torus, where ultraviolet and optical radiation from the accretion disk is absorbed and reprocessed into the infrared (Lutz et al. 2004). The intrinsic 2–10 keV X-ray luminosity ($L_{\rm X}$) probes the primary coronal emission produced by Compton up-scattering of disk photons in a hot, optically thin plasma above the accretion disk (Fabian et al. 2015). While the MIR luminosity is relatively insensitive to line-of-sight absorption (e.g. Hickox & Alexander 2018) – although some anisotropy due to torus geometry may remain present (e.g. Pier & Krolik 1992) – the X-ray emission can be strongly suppressed by intervening material. This allows deviations from known MIR–X-ray relations to reveal the presence of heavy obscuration or intrinsically weak quasars. The combination of these bands is sensitive to obscuration, bolometric output, and X-ray weakness in AGNs (Gandhi et al. 2009; Stern 2015).

3.2.1. MIR information

The SPIDERS catalogue provides cross-matched WISE photometry. We used the W1 (3.4 µm), W2 (4.6 µm), and W3 (12 µm) bands, given as Vega magnitudes, and converted them to flux densities using the zero-point values $F_{\nu0,\,\rm W1} = 309.504$ Jy, $F_{\nu0,\,\rm W2} = 171.787$ Jy and $F_{\nu0,\,\rm W3} = 31.674$ Jy (Jarrett et al. 2011):

$$F = F_{\nu0} \cdot 10^{-0.4 F_{\rm Vega}}. \tag{5}$$

For each source, we fitted a power-law spectral energy distribution (SED), $F_\nu \propto \nu^\alpha$, to the observed WISE W1–W3 photometry, convolving the model with the official WISE relative spectral response curves (Wright et al. 2010). This approach is consistent with previous studies of AGN MIR SEDs (e.g. Assef et al. 2015) and allowed us to estimate the rest-frame 6µm luminosity, $\nu L\nu(6\,\mu\text{m})$, taking into account the full bandpass and source redshift. WISE photometry also provides an independent diagnostic of AGN activity. The colour $W1 - W2$ traces the relative contribution of the AGN to the total bolometric luminosity of the host galaxy. A redder value indicates a stronger AGN component (Stern et al. 2012; Blecha et al. 2018). A colour cut of $(W1 - W2) > 0.8$ identifies sources in which the AGN contributes $\gtrsim 30\%$ to the total bolometric luminosity while $(W1 - W2) > 0.5$ corresponds to AGN fractions of $\gtrsim$10% (Stern et al. 2012). Combining these results with $(W2 - W3) > 2.2$ yields a two-colour selection with approximately 90% completeness for moderate luminosities ($L_{\rm AGN} > 10^{44}$ erg s^{-1}) up to $z \approx 0.5$ and nearly 100% completeness for luminous AGNs ($L_{\rm AGN} > 10^{45}$ erg s^{-1}) up to $z \approx 1$ (Blecha et al. 2018). We tested our sample and found an overall completeness of 90%, which increases to 95% when excluding quasars with $\nu L\nu(6\,\mu\text{m}) < 10^{44}$ erg s^{-1} at $z < 0.5$. These numbers demonstrate that the majority of our quasars have a dominant AGN contribution in the MIR, suggesting that $\nu L\nu(6\,\mu\text{m})$ predominantly traces the nuclear emission rather than host-galaxy light. In our sample, the MIR luminosity $\nu L\nu(6\,\mu\text{m})$ spans $1.7 \cdot 10^{42}$ erg s^{-1} – $7.4 \cdot 10^{46}$ erg s^{-1}.

3.2.2. X-ray information

For the analysis of the observed 0.2–2.3 keV fluxes from eROSITA, we used XSPEC v12.15.1 (HEASoft 6.32; Arnaud 1996) on the SciServer computing platform [2], which provides cloud-based access to HEASoft tools. As suggested in Liu et al. (2022), we used only sources with a detection likelihood >10 (Appendix B). The observed fluxes were modelled with an absorbed power-law model (phabs*powerlaw), where phabs accounts for Galactic absorption and powerlaw for a power-law continuum. Galactic H I column densities were obtained from the HI4PI map (HI4PI Collaboration 2016). The photon index Γ for non-blazar AGNs was fixed to a canonical value of $\Gamma = 1.8$, which is representative of the typical AGN X-ray spectrum (Nandra & Pounds 1994; Ricci et al. 2017). The model was used to derive rest-frame 2–10 keV luminosities ($L_{\rm X}$) from the

[2] sciserver.org

observed 0.2–2.3 keV fluxes. For the eROSITA Final Equatorial Depth Survey (eFEDS) sample, Liu et al. (2022) indicate a selection bias for soft-band-dominated sources and that the selected eFEDS sample is centred around $\Gamma \approx 2.0$. As an additional consistency check, we also derived the rest-frame 2–10 keV luminosities assuming a photon index of $\Gamma = 2.0$. Compared with the adopted $\Gamma = 1.8$ model, the inferred luminosities decrease by approximately 0.1 dex. We therefore conclude that adopting $\Gamma = 1.8$ provides a conservative upper limit on the estimated rest-frame 2–10 keV luminosities. In our sample, the X-ray luminosity L_X spans $8.8 \cdot 10^{41}$ erg s^{-1} – $1.6 \cdot 10^{46}$ erg s^{-1}.

3.2.3. Quantifying the MIR-normalised X-ray deficit

To quantify deviations from the expected MIR–X-ray relation, we defined ΔL_X as the signed orthogonal distance from the observed point $(x, y) = (\log \nu L\nu(6\,\mu\text{m}), \log L_X)$ to the relation $y = 40.981 + 1.024x' - 0.047x'^2$ of Stern (2015), with $x' = \log\left(\frac{\nu L\nu(6\,\mu\text{m})}{10^{41}\,\text{erg s}^{-1}}\right) = x - 41$. This choice accounts for intrinsic scatter in both variables and provides an unbiased estimate of deviation, whereas the vertical distance would assume all scatter lies along the L_X axis and could bias the inferred weakness for steep relations. Formally, we parametrised points along the relation by u (the value of $\log \nu L\nu(6\,\mu\text{m})$ corresponding to the closest point on the relation) and minimised the squared distance

$$D^2(u) = (u - x)^2 + (f(u) - y)^2. \quad (6)$$

Solving $dD^2/du = 0$ yields $u_{\min}$, from which we computed the orthogonal distance $\Delta L_X = \sqrt{D^2(u_{\min})}$ measured as a logarithmic luminosity distance (dex). We assigned a negative sign to sources located under the MIR–X-ray relation and a positive sign to sources above the relation. Therefore, negative ΔL_X values correspond to MIR-normalised X-ray deficits, while positive values indicate excess X-ray emission relative to the relation. This allowed us to quantify the deviation from the expected MIR–X-ray relation in a single parameter, which we use throughout the following sections to evaluate connections between X-ray properties, black hole masses, and outflow strength. In this work, we refer to sources with negative ΔL_X values as exhibiting an observed MIR-normalised X-ray deficit (or X-ray weakness), meaning that their observed X-ray luminosity is lower than expected from the MIR–X-ray relation. It therefore represents an observational measure of X-ray suppression rather than a direct diagnostic of the intrinsic X-ray emission mechanism. Such a deficit may arise from different physical processes, including absorption along the line of sight, intrinsic variations in coronal emission, or a combination of both. We additionally investigated possible obscuration signatures using the MIR-to-optical luminosity ratio $\nu L\nu(6\,\mu\text{m})/L_{5100}$, which may provide information on dust extinction and covering-factor variations (e.g. Maiolino et al. 2007). The majority of sources (82%) do not show strongly elevated ratios with $\nu L\nu(6\,\mu\text{m})/L_{5100} < 5$, although a subset may be affected by moderate obscuration. During the derivation of L_X, we did not explicitly account for possible contamination from soft-excess (e.g. Ross & Fabian 1993; Done et al. 2012; Petrucci et al. 2018) or scattered emission. As a result, the inferred X-ray luminosity may overestimate the contribution from the primary hard X-ray continuum. Consequently, the derived ΔL_X values provide conservative estimates of the degree of X-ray suppression, as any overestimation of L_X would reduce the apparent X-ray weakness. We therefore used ΔL_X to identify statistical trends within the sample. A detailed spectral analysis, including constraints on absorption and the intrinsic X-ray spectrum, would be required to determine the physical origin and exact magnitude of the X-ray weakness.

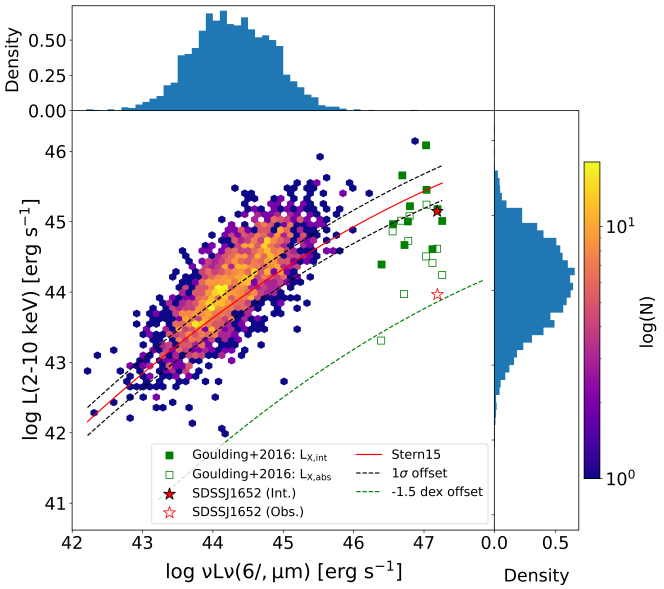


Fig. 2. Density distribution of MIR and X-ray luminosities for our 2119 quasars. The marginal distributions of both luminosities are shown along the axes. The solid red line denotes the Stern (2015) relation, and the dashed green line represents the expected suppression corresponding to $N_H = 10^{24}$ cm^{-2} (Zou et al. 2025). The dashed black lines show ±0.25 dex. We also included the observed ERQs with high-velocity outflows from Goulding et al. (2018) and SDSSJ1652 from Ishikawa et al. (2021), both with $1.5 < z < 3$. The filled symbols represent the intrinsic X-ray luminosity, and the empty symbols represent the absorbed luminosity. This figure highlights the distribution of the full sample and the prevalence of sources with MIR-normalised X-ray deficits.

4. Results and discussion

4.1. MIR and X-ray relation

Several studies have investigated the correlation between X-ray and MIR luminosities in AGNs over a wide luminosity range (~10^{42}–10^{47} erg s^{-1}, Lutz et al. 2004; Gandhi et al. 2009; Stern 2015; Chen et al. 2017). At low luminosities, the relation is approximately linear in log–log space, while at high luminosities it flattens. Fig. 2 shows our sample together with the relation shown in Stern (2015). To illustrate the effect of potential strong obscuration, we included a −1.5 dex offset, corresponding to an obscuration column of $N_H = 10^{24}$ cm^{-2} (Zou et al. 2025).

The scatter of our data around the Stern (2015) relation is $^{+0.26}_{-0.23}$ dex, which is broadly consistent with the intrinsic dispersion of approximately 0.3 dex reported by Carroll et al. (2023). While more quasars exhibit a positive ΔL_X than a negative one, the extreme positive outliers are fewer than the sources with MIR-normalised X-ray deficits. However, all sources with negative ΔL_X values remain within the 1.5 dex suppression expected for Compton-thick absorption. We further investigated the dependence of the X-ray-to-MIR luminosity ratio on MIR luminosity (Fig. 3). We find a systematic decrease in $L_X/\nu L\nu(6\,\mu\text{m})$ with increasing $\nu L\nu(6\,\mu\text{m})$ (linear-fit slope b = –0.195, Pearson $r = -0.275$, $p < 10^{-37}$), indicating that the X-ray luminosity increases sub-linearly with MIR luminosity. Such a behaviour is consistent with previous studies of the MIR-X-ray relation, which find a slope smaller than unity (e.g. Gandhi et al. 2009;

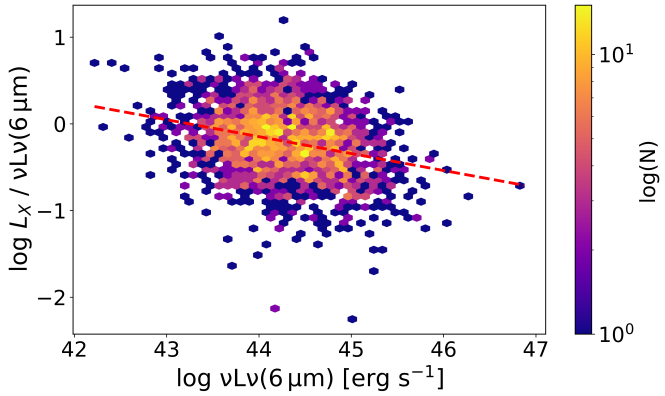


Fig. 3. X-ray-to-MIR luminosity ratio as a function of MIR luminosity for the quasar sample. The red line shows the best-fitting linear relation, indicating a statistically significant decrease in $L_X/\nu L\nu(6\,\mu m)$ with increasing $\nu L\nu(6\,\mu m)$($p < 10^{-37}$).

Stern et al. 2012), implying a relative decrease in X-ray emission at higher luminosities.

A comparison between ΔL_X and L_X reveals a significant positive correlation, indicating that the slope of the Stern (2015) relation is flatter and systematically lower than our results for the SPIDERS quasars. The assumed photon index of $\Gamma = 2.0$ from their calibration may account for part of the vertical offset, but it does not reproduce the discrepancy in slope. This mismatch suggests that the Stern (2015) relation was calibrated on broad-line, unobscured quasars, whereas the SPIDERS sample spans a broader range of obscuration and a wider diversity of host-galaxy contribution (Aydar et al. 2025). The flux-limited nature of the eROSITA survey introduces a selection bias towards X-ray brighter sources, since intrinsically X-ray weak quasars are less likely to satisfy the detection threshold. To investigate whether this selection affects our results, we repeated our analysis including sources with lower eROSITA detection likelihood values (Appendix B). This test confirms that the detection likelihood threshold introduces a mild bias in the ΔL_X distribution. The additional lower-significance sources show a shift towards lower ΔL_X values, consistent with the expectation that X-ray weaker and lower-luminosity sources are preferentially excluded by a flux-limited selection. However, the inclusion of these sources does not qualitatively change the observed trends. In particular, the $L_X/\nu L\nu(6\,\mu m)$ relation and the association between stronger ionised gas outflows and reduced X-ray emission remain consistent with the main sample. Therefore, while the detection threshold affects the detailed composition of the sample, it does not qualitatively alter the interpretation of our results. Consequently, the MIR-normalised X-ray deficits identified within the detected sample should be regarded as conservative. Adopting a relation that more accurately reflects the observed SPIDERS sample, particularly in the range $43 < \log(\nu L\nu(6\,\mu m)/\mathrm{erg\,s^{-1}}) < 45$, would further reduce the mean value $\Delta L_X = (0.26 \pm 0.22)$ dex, thereby increasing both the number and the significance of sources with MIR-normalised X-ray deficits identified in our sample. In combination with the results from Sect. 3.2.2, we interpret our measurements as representing an upper limit on ΔL_X, since both a tighter luminosity relation and a lower intrinsic X-ray luminosity would further reduce ΔL_X.

4.2. Mass and colour in the MIR–X-ray plane

We additionally examined the MIR–X-ray relation in the context of host-galaxy and black hole properties (top and middle panel in Fig. 4). The $W1 - W2$ colour becomes redder with increasing luminosity, consistent with an increasing fractional contribution of hot, AGN-heated dust relative to stellar emission (Stern et al. 2012; Assef et al. 2013). While WISE magnitudes are not k-corrected and therefore retain a moderate redshift dependence, the observed trend is significantly stronger than expected from redshift effects alone (Stern 2015; Assef et al. 2018). This behaviour supports the interpretation that more luminous quasars are increasingly dominated by AGN emission in the MIR, with reduced host contamination.

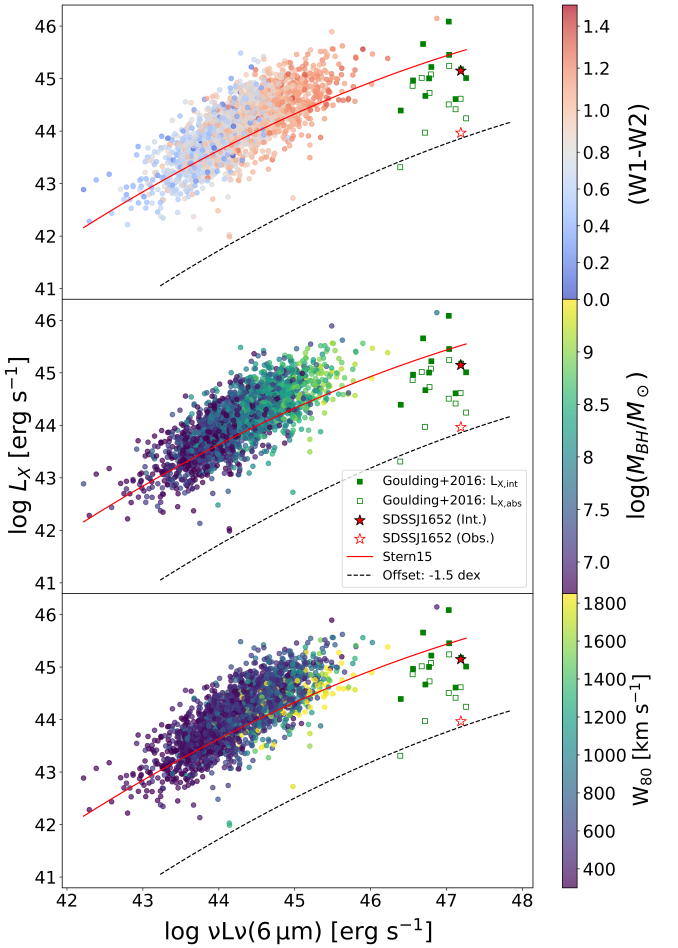


Fig. 4. Similar to Fig. 2 but colour-coded with the W1–W2 colour (top), the $H\beta$ based virial black hole mass (middle), and the outflow strength (bottom). Unlike Fig. 2, this figure is not a density plot. The observed trends highlight increasing AGN dominance and mass with MIR luminosity.

A similar positive trend is observed between luminosity and black hole masses. Virial black hole masses are derived from the broad Hβ emission line, which traces the dynamics of the BLR. In the single-epoch framework, $M_{\rm BH}$ scales with both the FWHM of Hβ and the continuum luminosity at 5100 Å (e.g. Greene & Ho 2005; Vestergaard & Peterson 2006; Shen 2013). Since the optical continuum luminosity correlates with the bolometric output of AGNs, higher-luminosity-systems are naturally associated with more massive black holes (Croom 2011). This behaviour highlights the close connection between MIR emission, X-ray production, and the central engine. More massive and rapidly accreting black holes are associated with brighter accretion disks, enhanced coronal emission, and a more prominent

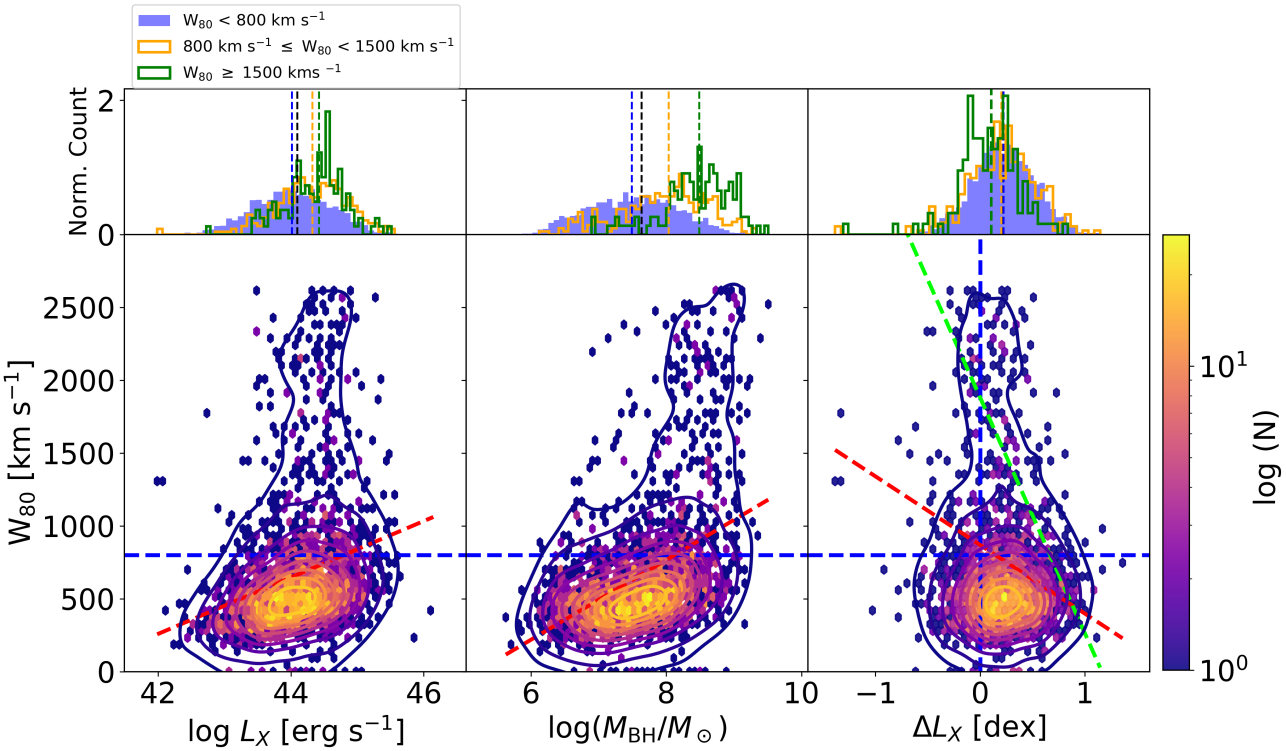


Fig. 5. Bottom panels: non-parametric velocity width W_{80} as a function of the rest-frame 2–10 keV X-ray luminosity (left), the virial black hole mass (centre), and the MIR-normalised X-ray offset ΔL_X (right). The red line indicates the best-fitting linear relation for the full sample in all panels. The lime-green line in the right panel shows the best-fitting linear relation for sources with $W_{80} > 800\,\mathrm{km\,s^{-1}}$. Top panels: distribution of AGNs with extreme ($W_{80} \geq 1500\,\mathrm{km\,s^{-1}}$, green), moderate ($1500\,\mathrm{km\,s^{-1}} > W_{80} \geq 800\,\mathrm{km\,s^{-1}}$, orange), and no ($W_{80} < 800\,\mathrm{km\,s^{-1}}$, blue) outflow signatures as a function of L_X (left), M_{BH} (centre), and ΔL_X (right). The vertical dashed black, green, orange, and blue lines indicate the median values of the full, extreme-outflow, moderate-outflow, and non-outflow populations, respectively. The corresponding values are listed in Table A.1.

AGN-heated dust component, jointly increasing both X-ray and MIR luminosity.

4.3. Ionised outflows

Fig. 5 presents the behaviour of L_X, M_{BH} and ΔL_X as a function of the non-parametric velocity width W_{80}. For L_X and M_{BH}, we compared our results with previous studies (e.g. Harrison et al. 2016; Perna et al. 2017), which identified positive correlations between outflow velocity, AGN luminosities, and black hole mass. The dashed red lines represent least-squares linear regressions obtained by fitting W_{80} as the dependent variable according to

$$W_{80} = a \cdot x + b, \tag{7}$$

where x denotes log L_X, M_{BH} or ΔL_X. The best-fit parameters are summarised in Table 1. We find a similar trend in our sample. Both the observed (non-absorption corrected) X-ray luminosity and the virial black hole mass increase with W_{80}, consistent with the positive slopes obtained for the full sample (Table 1). Restricting the analysis to quasars with $W_{80} > 800\,\mathrm{km\,s^{-1}}$ shows that the correlation with black hole mass remains significant, whereas the correlation with observed X-ray luminosity becomes much weaker. Consistent with Perna et al. (2017) and Fiore et al. (2017), quasars exhibiting ionised outflows are, on average, more X-ray luminous and host more massive black holes than the population with non-prominent outflows.

With ΔL_X for 2119 quasars, we can now statistically investigate how ionised outflows relate to MIR-normalised X-ray deficits. Previous evidence relied mainly on individual extreme sources or smaller samples. The quasars observed by Goulding et al. (2018) are among the most luminous quasars observed at $z \sim 2$ and exhibit exceptionally strong galaxy-scale outflows. Deep Chandra observations revealed heavy, in some cases Compton-thick, obscuration in these sources, while their intrinsic X-ray luminosity is consistent with the MIR-X-ray relation of Stern (2015). Similar conclusions are drawn by Ishikawa et al. (2021) for the quasar SDSSJ1652 at $z = 2.94$. According to both studies, ERQs host powerful winds despite appearing as X-ray weak in the observed frame. Detailed X-ray analyses indicate that their reduced observed X-ray emission is consistent with substantial obscuration, while their intrinsic X-ray luminosities remain consistent with MIR–X-ray relations. This distinguishes their apparent X-ray deficit from a scenario in which the X-ray corona itself produces intrinsically weaker emission than expected for typical quasars.

While these results provide compelling evidence that strong outflows can coexist with intrinsically normal X-ray emission, they are based on rare, highly luminous systems. Our analysis extends this investigation to a larger and representative sample of SPIDERS quasars at $z < 0.95$, enabling a population-level assessment of how X-ray weakness relates to ionised outflow strength across a broad range of luminosities and physical conditions.

A first inspection of the bottom panel of Fig. 4 shows that for a given MIR luminosity, quasars with larger W_{80} values tend to occupy the lower L_X region at $\nu L\nu(6\,\mu\mathrm{m}) > 10^{45}\,\mathrm{erg\,s^{-1}}$. A closer examination of ΔL_X as a function of W_{80} (Fig. 5, bottom right panel) reveals an almost uniform distribution in ΔL_X,

Table 1. Linear-fit parameters for the relations between the W_{80} velocity width and the X-ray luminosity, black hole mass, and MIR-normalised X-ray offset.

Relation	Sample	a	b	r	p
W_{80}– $\log L_X$	Full	193.52	–7868.25	0.263	2.22×10^{-34}
	$W_{80} < 800\,\mathrm{km\,s^{-1}}$	79.75	–3019.28	0.329	1.71×10^{-43}
	$W_{80} > 800\,\mathrm{km\,s^{-1}}$	42.94	–574.08	0.042	3.91×10^{-1}
W_{80}– $\log M_{BH}$	Full	273.90	–1423.91	0.441	1.45×10^{-100}
	$W_{80} < 800\,\mathrm{km\,s^{-1}}$	67.99	–18.47	0.313	3.21×10^{-39}
	$W_{80} > 800\,\mathrm{km\,s^{-1}}$	327.42	–1322.14	0.399	9.35×10^{-18}
W_{80}– ΔL_X	Full	–470.86	869.39	–0.099	6.20×10^{-6}
	$W_{80} < 800\,\mathrm{km\,s^{-1}}$	14.03	499.54	0.062	1.11×10^{-2}
	$W_{80} > 800\,\mathrm{km\,s^{-1}}$	–1617.01	1879.85	–0.192	6.37×10^{-5}

Notes. The relations are shown in Fig. 5 and take the form $W_{80} = a\,x + b$, where x represents $\log L_X$, $\log M_{BH}$, or ΔL_X. The slope a is given in kilometres per second per dex for the logarithmic quantities, whereas b is given in kilometres per second. The table also lists the Pearson's correlation coefficient (r) and the corresponding p value.

spanning roughly ±1 dex, for quasars with $W_{80} < 800\,\mathrm{km\,s^{-1}}$ ($N = 1691$), with no obvious visual trend. Although a formal correlation is detected (Pearson $r = 0.062$, Spearman $\rho = 0.073$, $p = 1 \times 10^{-2}$), the correlation coefficients are extremely small, indicating a negligible effect size despite the statistical significance enabled by the large sample size. The inferred trend therefore appears to have little physical relevance, with the observed scatter dominating over any dependence on W_{80}. We therefore conclude that, for quasars lacking strong outflows, any connection between the X-ray emission and the kinematics of the ionised gas is, at most, weak. In contrast, quasars exhibiting clear outflow signatures ($W_{80} > 800\,\mathrm{km\,s^{-1}}$, $N = 428$) display a weak but highly significant anti-correlation between ΔL_X and W_{80} ($r \approx \rho \approx -0.192$, $p = 6 \times 10^{-5}$). This indicates that quasars with increasingly powerful outflows tend to exhibit suppressed X-ray emission, although the substantial scatter shows that the effect is modest. Consistently, the ΔL_X histogram shows that outflow sources preferentially populate the low-ΔL_X tail of the distribution. To ensure that this trend is not dominated by the three outliers ($\Delta L_X < -1.1$), we excluded them and saw the same trends with similar statistics. To further illustrate this effect, we separately highlight strong outflows ($W_{80} > 1500\,\mathrm{km\,s^{-1}}$, $N = 132$), which exhibit lower mean ΔL_X values (0.085 ± 0.025 dex) than quasars with moderate outflows (0.199 ± 0.019 dex) in the range $800\,\mathrm{km\,s^{-1}} < W_{80} < 1500\mathrm{km\,s^{-1}}$, where the uncertainties denote the standard error of the mean. A Mann-Whitney U test confirms that the two distributions differ significantly ($U = 15\,116$, $p = 1.8 \times 10^{-4}$). However, the histograms in the upper-right panel in Fig. 5 show substantial overlap between the two populations, suggesting a modest shift towards lower ΔL_X values rather than a clear separation between strong and moderate outflows.

Taken together, these results suggest that quasars hosting fast ionised outflows are preferentially found among sources with weaker X-ray emission relative to their MIR-luminosity. This behaviour is qualitatively similar to the connection between UV outflow indicators and UV-normalised X-ray emission reported previously (e.g. Brandt et al. 2000; Laor & Brandt 2002), where stronger UV outflows are associated with weaker relative X-ray emission. However, the observed X-ray weakness does not uniquely identify the underlying physical mechanism, as it may result from intrinsic changes in the corona, absorption along the line of sight, or a combination of both. In addition, our sample reveals a clear luminosity dependence, such that the maximum outflow velocities generally increase with AGN luminosity, consistent with the luminosity-dependent velocity envelope reported for UV outflows. While quasars without prominent outflow signatures show no physically meaningful dependence of ΔL_X on gas kinematics, quasars with $W_{80} > 800\,\mathrm{km\,s^{-1}}$ exhibit a noticeably steeper negative relation between ΔL_X and W_{80} (Table 1). In contrast, the positive relation between observed X-ray luminosity and W_{80} largely disappears within the outflow population, whereas the correlation with black hole mass remains significant.

The origin of this suppression remains uncertain. Possible explanations include intrinsic changes in coronal emission and/or absorption associated with the outflowing material (e.g. Luo et al. 2013; Ricci et al. 2017; Goulding et al. 2018). In radiatively driven wind scenarios, reduced X-ray and EUV radiation close to the nucleus can act as an effective shielding mechanism, preventing overionisation of the outflowing gas and facilitating the launch of fast radiatively driven (line-driven) winds (e.g. Murray et al. 1995; Proga et al. 2000; Proga & Kallman 2004; Leighly et al. 2007). The large sample provides statistical evidence for an association between AGN energetic output, black hole mass and relative X-ray suppression. This extends earlier results to the broader SPIDERS quasar population.

5. Summary and conclusions

In this paper, we analysed the properties of 2119 quasars at $z < 0.95$. We used the optical SDSS-V spectra to extract the $H\beta$ and [O III] λ5007 emission lines with the spectral fitting tool `BADASS3`, which allowed estimation of virial black hole mass and characterisation of ionised gas kinematics, including outflow strength. Additionally, we used WISE and eROSITA to measure the rest-frame 6 µm and the 2–10 keV luminosities. Comparing these luminosities with the MIR–X-ray relation from Stern (2015), we defined the MIR-normalised X-ray offset, ΔL_X, which quantifies the observed X-ray deficit relative to the expected relation. The main results of our analysis can be summarised as follows:

– The virial black hole masses span $5.65 < \log(M_{BH}/M_\odot) < 9.51$, with a mean of $\log(M_{BH}/M_\odot) = 7.55$. The ionised outflow strength, traced by the non-parametric W_{80}, reaches up to $\sim 2500\,\mathrm{km\,s^{-1}}$;
– We confirm previously reported positive trends with X-ray luminosity, black hole mass, and outflow strength (e.g.

Vestergaard & Peterson 2006; Perna et al. 2017; Fiore et al. 2017). Quasars exhibiting outflow signatures ($W_{80} \geq 800\,\mathrm{km\,s^{-1}}$) are, on average, more X-ray luminous and host more massive black holes than quasars without prominent outflows. While the correlation between W_{80} and observed X-ray luminosity becomes much weaker within the outflow population, the correlation with black hole mass remains significant;
- For the first time in a large sample of 2119 quasars, we identify a statistically significant anti-correlation between ΔL_X (the observed X-ray suppression relative to the MIR–X-ray relation) and W_{80} among quasars with clear outflow signatures, i.e. stronger ionised outflows are preferentially associated with sources exhibiting larger MIR-normalised X-ray deficits. In contrast, quasars without outflow signatures show no physically meaningful dependence of ΔL_X on ionised-gas kinematics;
- While our data do not allow us to distinguish between intrinsic changes in the X-ray emitting corona and suppression due to absorption, the maximum observed X-ray deficits ($\lesssim -1.5$ dex) are comparable to the suppression expected from heavily obscured, potentially Compton-thick sources (e.g. Ishikawa et al. 2021). Consequently, absorption remains a plausible explanation for at least part of the observed X-ray suppression, although additional X-ray spectroscopic data is required to determine its relative importance. Furthermore, strongly absorbed quasars may preferentially fall below the detection threshold of eROSITA, implying that selection effects could bias the observed sample against the most heavily obscured objects;
- The substantial population of quasars with strong outflow signatures and MIR-normalised X-ray deficits identified in this work represents a promising target set for future observations of these sources. Spatially resolved observations can probe the morphology and spatial extent of the outflows, thereby linking nuclear activity to feedback processes operating on the host-galaxy scales. A follow-up paper is planned in which a larger set of sources with additional X-ray spectroscopy information will be used to obtain the intrinsic hard X-ray luminosities and absorption properties of the observed quasars. Through this, we will be able to distinguish between intrinsic X-ray suppression and absorption-driven X-ray deficits.

Overall, this large statistical sample provides robust observational evidence that quasars with fast ionised outflows preferentially exhibit suppressed observed X-ray emission relative to the MIR–X-ray relation. Although the physical origin of this suppression cannot be determined from the present data alone, the results provide important constraints for models linking AGN accretion, X-ray emission, and radiatively driven ionised outflows.

Acknowledgements. Funding for the Sloan Digital Sky Survey V has been provided by the Alfred P. Sloan Foundation, the Heising-Simons Foundation, the National Science Foundation, and the Participating Institutions. SDSS acknowledges support and resources from the Center for High-Performance Computing at the University of Utah. SDSS telescopes are located at Apache Point Observatory, funded by the Astrophysical Research Consortium and operated by New Mexico State University, and at Las Campanas Observatory, operated by the Carnegie Institution for Science. The SDSS web site is www.sdss.org. SDSS is managed by the Astrophysical Research Consortium for the Participating Institutions of the SDSS Collaboration, including the Carnegie Institution for Science, Chilean National Time Allocation Committee (CNTAC) ratified researchers, Caltech, the Gotham Participation Group, Harvard University, Heidelberg University, The Flatiron Institute, The Johns Hopkins University, L'Ecole polytechnique fédérale de Lausanne (EPFL), Leibniz-Institut für Astrophysik Potsdam (AIP), Max-Planck-Institut für Astronomie (MPIA Heidelberg), Max-Planck-Institut für Extraterrestrische Physik (MPE), Nanjing University, National Astronomical Observatories of China (NAOC), New Mexico State University, The Ohio State University, Pennsylvania State University, Smithsonian Astrophysical Observatory, Space Telescope Science Institute (STScI), the Stellar Astrophysics Participation Group, Universidad Nacional Autónoma de México, University of Arizona, University of Colorado Boulder, University of Illinois at Urbana-Champaign, University of Toronto, University of Utah, University of Virginia, Yale University, and Yunnan University. This work is based on data from eROSITA, the soft X-ray instrument aboard SRG, a joint Russian-German science mission supported by the Russian Space Agency (Roskosmos), in the interests of the Russian Academy of Sciences represented by its Space Research Institute (IKI), and the Deutsches Zentrum für Luft- und Raumfahrt (DLR). The SRG spacecraft was built by Lavochkin Association (NPOL) and its subcontractors, and is operated by NPOL with support from the Max-Planck Institute for Extraterrestrial Physics (MPE). The development and construction of the eROSITA X-ray instrument was led by MPE, with contributions from the Dr. Karl Remeis Observatory Bamberg, the University of Hamburg Observatory, the Leibniz Institute for Astrophysics Potsdam (AIP), and the Institute for Astronomy and Astrophysics of the University of Tübingen, with the support of DLR and the Max Planck Society. The Argelander Institute for Astronomy of the University of Bonn and the Ludwig Maximilians Universität Munich also participated in the science preparation for eROSITA. RJA was supported by FONDECYT grant number 1231718 and by the ANID BASAL project FB210003. ALR acknowledges support from a Leverhulme Early Career Fellowship. The authors acknowledge the anonymous reviewer who provided many useful suggestions for improving the paper.

References

Albán, M., Wylezalek, D., Comerford, J. M., et al. 2024, A&A, 691, A124
Alexander, D., & Hickox, R. 2012, NewAR, 56, 93
Arnaud, K. A. 1996, in Astronomical Society of the Pacific Conference Series, 101, Astronomical Data Analysis Software and Systems V, eds. G. H. Jacoby, & J. Barnes, 17
Assef, R. J., Stern, D., Kochanek, C. S., et al. 2013, ApJ, 772, 26
Assef, R. J., Eisenhardt, P. R. M., Stern, D., et al. 2015, ApJ, 804, 27
Assef, R. J., Prieto, J. L., Stern, D., et al. 2018, ApJ, 866, 26
Aydar, C., Merloni, A., Dwelly, T., et al. 2025, A&A, 698, A132
Banerji, M., Alaghband-Zadeh, S., Hewett, P. C., et al. 2015, MNRAS, 447, 3368
Baskin, A., Laor, A., & Stern, J. 2014, MNRAS, 445, 3025
Benson, A. J., Bower, R. G., Frenk, C. S., et al. 2003, ApJ, 599, 38
Bertemes, C., Wylezalek, D., Rupke, D. S. N., et al. 2025, A&A, 693, A176
Blecha, L., Snyder, G. F., Satyapal, S., et al. 2018, MNRAS, 478, 3056
Bolton, A. S., Schlegel, D. J., Aubourg, É., et al. 2012, AJ, 144, 144
Bowen, I. S., & Vaughan, Jr., A. H. 1973, Appl. Opt., 12, 1430
Brandt, W. N., & Alexander, D. M. 2015, A&A Rev., 23
Brandt, W. N., Laor, A., & Wills, B. J. 2000, ApJ, 528, 637
Calderone, G., Nicastro, L., Ghisellini, G., et al. 2017, MNRAS, 472, 4051
Carroll, C. M., Ananna, T. T., Hickox, R. C., et al. 2023, ApJ, 950, 127
Chen, C.-T. J., Hickox, R. C., Goulding, A. D., et al. 2017, ApJ, 837, 145
Comparat, J., Merloni, A., Dwelly, T., et al. 2020, A&A, 636, A97
Croom, S. M. 2011, ApJ, 736, 161
Dimitrijević, M. S., Popović, L. Č., Kovačević, J., et al. 2007, MNRAS, 374, 1181
Done, C., Davis, S. W., Jin, C., et al. 2012, MNRAS, 420, 1848
Duras, F., Bongiorno, A., Ricci, F., et al. 2020, A&A, 636, A73
Dwelly, T., Salvato, M., Merloni, A., et al. 2017, MNRAS, 469, 1065
Eisenhardt, P. R. M., Wu, J., Tsai, C.-W., et al. 2012, ApJ, 755, 173
Fabian, A. C. 1999, MNRAS, 308, L39
Fabian, A. C., Lohfink, A., Kara, E., et al. 2015, MNRAS, 451, 4375
Fiore, F., Feruglio, C., Shankar, F., et al. 2017, A&A, 601, A143
Fitzpatrick, E. L. 1999, PASP, 111, 63
Gandhi, P., Horst, H., Smette, A., et al. 2009, A&A, 502, 457
Gibson, R. R., Jiang, L., Brandt, W. N., et al. 2009, ApJ, 692, 758
Goulding, A. D., Zakamska, N. L., Alexandroff, R. M., et al. 2018, ApJ, 856, 4
Greene, J. E., & Ho, L. C. 2005, ApJ, 630, 122
Gunn, J. E., Siegmund, W. A., Mannery, E. J., et al. 2006, AJ, 131, 2332
Hamann, F., Zakamska, N. L., Ross, N., et al. 2017, MNRAS, 464, 3431
Harrison, C. M., Alexander, D. M., Mullaney, J. R., et al. 2014, MNRAS, 441, 3306
Harrison, C. M., Alexander, D. M., Mullaney, J. R., et al. 2016, MNRAS, 456, 1195
Harrison, C. M., Costa, T., Tadhunter, C. N., et al. 2018, Nat. Astron., 2, 198
HI4PI Collaboration (Ben Bekhti, N., et al.) 2016, A&A, 594, A116
Hickox, R. C., & Alexander, D. M. 2018, ARA&A, 56, 625
Hiremath, P., Rankine, A. L., Aird, J., et al. 2025, MNRAS, 542, 2105

Hopkins, P. F., Hernquist, L., Cox, T. J., et al. 2006, ApJS, 163, 1
Hopkins, P. F., Hernquist, L., Cox, T. J., et al. 2008, ApJS, 175, 356
Ishikawa, Y., Goulding, A. D., Zakamska, N. L., et al. 2021, MNRAS, 502, 3769
Jarrett, T. H., Cohen, M., Masci, F., et al. 2011, ApJ, 735, 112
King, A. 2003, ApJ, 596, L27
Kollmeier, J. A., et al. 2026, AJ, 171, 52
Laor, A., & Brandt, W. N. 2002, ApJ, 569, 641
Leighly, K. M., Halpern, J. P., Jenkins, E. B., et al. 2007, ApJ, 663, 103
Liu, G., Zakamska, N. L., Greene, J. E., et al. 2013, MNRAS, 436, 2576
Liu, T., Buchner, J., Nandra, K., et al. 2022, A&A, 661, A5
Luo, B., Brandt, W. N., Alexander, D. M., et al. 2013, ApJ, 772, 153
Lusso, E., Comastri, A., Simmons, B. D., et al. 2012, MNRAS, 425, 623
Lutz, D., Maiolino, R., Spoon, H. W. W., et al. 2004, A&A, 418, 465
Madau, P., & Dickinson, M. 2014, ARA&A, 52, 415
Maiolino, R., Shemmer, O., Imanishi, M., et al. 2007, A&A, 472, L33
Marocco, F., Eisenhardt, P. R. M., Fowler, J. W., et al. 2021, ApJS, 253, 8
Menci, N., Fiore, F., Puccetti, S., et al. 2008, ApJ, 686, 219
Merloni, A., Lamer, G., Liu, T., et al. 2024, A&A, 682, A34
Murray, N., Chiang, J., Grossman, S. A., et al. 1995, ApJ, 451, 498
Nandra, K., & Pounds, K. A. 1994, MNRAS, 268, 405
Narayanan, D., Dey, A., Hayward, C. C., et al. 2010, MNRAS, 407, 1701
Perna, M., Lanzuisi, G., Brusa, M., et al. 2017, A&A, 603, A99
Petrucci, P.-O., Ursini, F., De Rosa, A., et al. 2018, A&A, 611, A59
Pier, E. A., & Krolik, J. H. 1992, ApJ, 399, L23
Predehl, P., Andritschke, R., Arefiev, V., et al. 2021, A&A, 647, A1
Proga, D., & Kallman, T. R. 2004, ApJ, 616, 688
Proga, D., Stone, J. M., & Kallman, T. R. 2000, ApJ, 543, 686
Pu, X., Luo, B., Brandt, W. N., et al. 2020, ApJ, 900, 141
Ricci, C., Ueda, Y., Koss, M. J., et al. 2015, ApJ, 815, L13
Ricci, C., Trakhtenbrot, B., Koss, M. J., et al. 2017, ApJS, 233, 17
Ross, R. R., & Fabian, A. C. 1993, MNRAS, 261, 74
Runnoe, J. C., Brotherton, M. S., & Shang, Z. 2012, MNRAS, 422, 478
Salvato, M., Wolf, J., Dwelly, T., et al. 2022, A&A, 661, A3
Salvato, M., Wolf, J., Dwelly, T., et al. 2025, A&A, 704, A344
SDSS Collaboration (Aghakhanloo, M., et al.) 2026, ApJS, 285, 9
Sexton, R. O., Matzko, W., Darden, N., et al. 2021, MNRAS, 500, 2871
Shen, Y. 2013, Bull. Astron. Soc. India, 41, 61
Shen, Y., Richards, G. T., Strauss, M. A., et al. 2011, ApJS, 194, 45
Silk, J., & Rees, M. J. 1998, A&A, 331, L1
Sim, S. A., Proga, D., Miller, L., et al. 2010, MNRAS, 408, 1396
Smee, S. A., Gunn, J. E., Uomoto, A., et al. 2013, AJ, 146, 32
Stern, D. 2015, ApJ, 807, 129
Stern, D., Assef, R. J., Benford, D. J., et al. 2012, ApJ, 753, 30
Tortosa, A., Zappacosta, L., Piconcelli, E., et al. 2024, A&A, 691, A235
Vazdekis, A., Sánchez-Blázquez, P., Falcón-Barroso, J., et al. 2010, MNRAS, 404, 1639
Véron-Cetty, M. P., Joly, M., & Véron, P. 2004, A&A, 417, 515
Vestergaard, M., & Peterson, B. M. 2006, ApJ, 641, 689
Wang, C., Luo, B., Brandt, W. N., et al. 2022, ApJ, 936, 95
Weymann, R. J., Morris, S. L., Foltz, C. B., et al. 1991, ApJ, 373, 23
Wright, E. L., Eisenhardt, P. R. M., Mainzer, A. K., et al. 2010, AJ, 140, 1868
Wu, Q., & Shen, Y. 2022, ApJS, 263, 42
Yu, Z., Brandt, W. N., Zou, F., et al. 2024, ApJ, 977, 210
Zappacosta, L., Piconcelli, E., Fiore, F., et al. 2023, A&A, 678, A201
Zou, F., Brandt, W. N., Gallo, E., et al. 2025, ApJ, 990, 94

Appendix A: Additional statistics for outflow populations

Table A.1: Median values for the full sample and the three ionised outflow populations.

Quantity	Full	No outflow $W_{80} < 800$	Moderate outflow $800 \leq W_{80} < 1500$	Extreme outflow $W_{80} \geq 1500$
$\log L_X$	44.10	44.01	44.37	44.42
$\log(M_{BH}/M_\odot)$	7.64	7.49	8.20	8.49
ΔL_X [dex]	0.21	0.22	0.17	0.11

Notes. The populations are divided according to their ionised outflow strength, traced by W_{80}. The no-outflow, moderate-outflow, and extreme-outflow populations correspond to $W_{80} < 800$, $800 \leq W_{80} < 1500$, and $W_{80} \geq 1500$, respectively, where W_{80} is expressed in km s^{-1}. The values are the medians of the distributions shown in the upper panels of Fig. 5.

Appendix B: Impact of the eROSITA detection-likelihood selection

The eROSITA sample used throughout this work was selected by requiring an X-ray detection likelihood of DET_LIKE > 10. This criterion was adopted to ensure reliable X-ray measurements and to minimise the fraction of sources with poorly constrained fluxes. However, such a selection may introduce a bias against intrinsically X-ray weak quasars, since sources with weak X-ray emission are less likely to exceed the detection threshold. To assess the potential impact of this selection, we repeated our analysis by including sources with lower detection likelihood values.

Relaxing the detection likelihood criterion adds 483 quasars to the sample, which we refer to as the 'mini sample'. A first look (Fig. B.1) reveals that the mini sample contains sources with lower X-ray luminosities in comparison to the main sample. This suggests that there are more X-ray weak sources. This can be seen in the left panel of Fig. B.2 which compares the X-ray weakness distribution as a function of W_{80}. The median X-ray weakness changes from 0.16 dex for the main sample to -0.02 dex for the mini sample. Thus, the mini sample shows a shift towards lower ΔL_X values compared whith the main sample, but it does not introduce a dominant population of strongly X-ray weak quasars. To investigate whether this difference affects the connection between X-ray weakness and ionised gas outflows, we compared the two samples as a function of W_{80}. The results are summarised in Table B.1. The mini sample shows a similar behaviour to the main sample, with quasars exhibiting broader [O III] profiles tending to have lower X-ray luminosities. In particular, quasars with strong outflows ($W_{80} > 1500$ km s^{-1}) have a median X-ray weakness of −0.24 dex in the mini sample, compared with 0.07 dex in the main sample. However, this bin contains only 13 objects and is therefore subject to substantial statistical uncertainties.

Finally, we repeated the comparison between X-ray and MIR luminosity (right panel of Fig. B.2). The Pearson correlation between $\log(L_X/\nu L\nu(6\,\mu m))$ and $\nu L\nu(6\,\mu m)$ remains significant for the mini sample ($r = -0.29$, $p = 5.0 \times 10^{-11}$), comparable to the correlation obtained for the main sample ($r = -0.22$, $p = 5.2 \times 10^{-25}$). Combining both samples results in $r = -0.20$ ($p = 7.9 \times 10^{-25}$), demonstrating that the inclusion of lower-significance detections does not qualitatively alter the observed luminosity dependence.

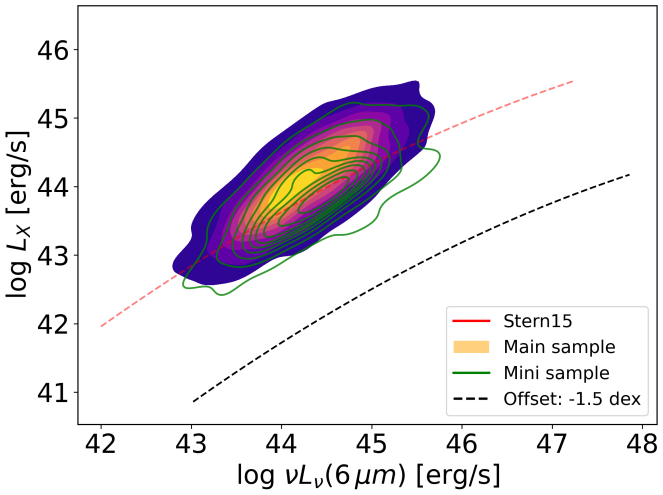


Fig. B.1: Distribution of sources on the log $\nu L\nu(6\,\mu m)$ vs L_X plane of sources with X-ray detection likelihood > 10 (main sample) and a detection likelihood < 10. The dashed red line represents the MIR–X-ray relation of Stern (2015), while the dashed black line indicates an offset of -1.5 dex from this relation.

Table B.1: Comparison of X-ray weakness between the main sample and the lower detection-likelihood mini sample.

Sample	N	median ΔL_X	mean ΔL_X
Main sample	2119	0.155	0.160
Mini sample	483	-0.024	0.015
$W_{80} < 800$ km s^{-1} (main)	1691	0.159	0.167
$W_{80} < 800$ km s^{-1} (mini)	417	-0.018	0.026
$800 < W_{80} < 1500$ km s^{-1} (main)	296	0.170	0.163
$800 < W_{80} < 1500$ km s^{-1} (mini)	53	-0.041	-0.005
$W_{80} > 1500$ km s^{-1} (main)	132	0.074	0.065
$W_{80} > 1500$ km s^{-1} (mini)	13	-0.242	-0.253

The relation between X-ray weakness and W_{80} is also not driven solely by the adopted detection threshold. For the combined sample, the Pearson correlation is weak for the full population ($r = -0.049$), but becomes stronger when considering sources with outflow signatures: $W_{80} > 800$ km s^{-1} gives $r = -0.16$ ($p = 3.8 \times 10^{-4}$). This behaviour is consistent with the trend found in the main sample and indicates that the observed connection between ionised gas outflows and reduced X-ray emission is not caused exclusively by the DET_LIKE > 10 selection.

Nevertheless, the lower detection-likelihood sources have less reliable X-ray measurements, and their inclusion introduces additional uncertainties. For this reason, we retain the DET_LIKE > 10 criterion for the main analysis. This test demonstrates that the main conclusions are not driven by the exclusion of marginal eROSITA detections.

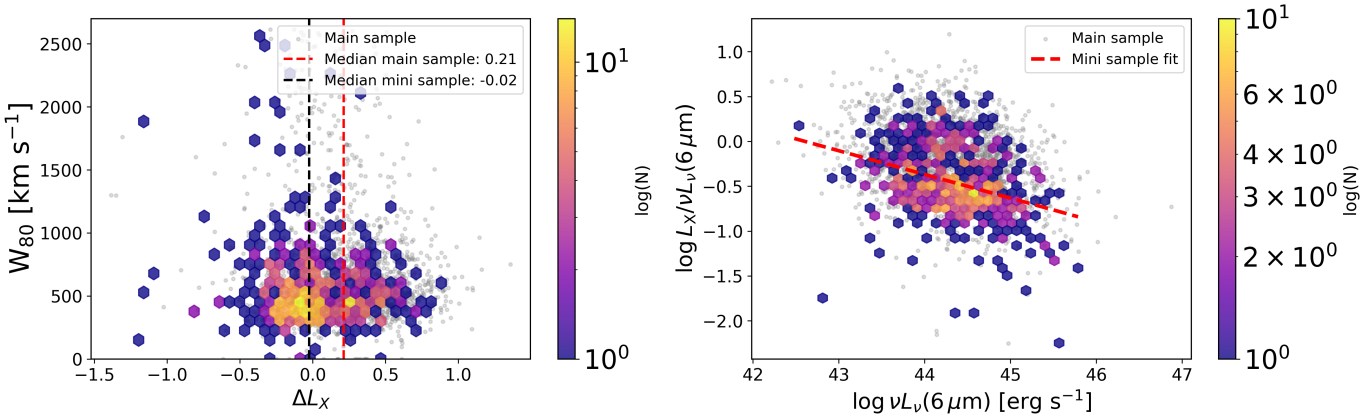


Fig. B.2: Impact of the eROSITA detection-likelihood selection on the derived relations. Left: X-ray weakness, defined as the offset from the adopted $L_X/\nu L\nu(6\,\mu m)$ relation, as a function of W_{80}. The main sample is shown in grey, while the additional lower detection-likelihood sources are shown as a density distribution. Right: Corresponding $L_X/\nu L\nu(6\,\mu m)$ vs $\nu L\nu(6\,\mu m)$ relation.

Appendix C: Comparison with qVAC

To assess the consistency of our spectral fitting results, we cross-matched our SPIDERS quasar sample with the qVAC catalogue and compared the derived black hole masses and ionised gas kinematics for the same 1291 objects. This comparison allows us to quantify systematic differences between the two fitting approaches and evaluate the reliability of the parameters used in this work. Fig. C.1 shows the comparison between the virial black hole masses derived in this work and those reported in the qVAC catalogue. The left panel compares our measurements with the catalogue values obtained using the original qVAC continuum luminosities, while the right panel shows the comparison after applying a host-galaxy correction to the 5100 Å luminosity. For the uncorrected comparison, our black hole masses show a systematic offset towards lower values, with a median difference of −0.21 dex and a mean offset of −0.30 dex. The scatter of the differences is 0.57 dex, corresponding to a root mean square (RMS) deviation of 0.65 dex. Despite this offset, the two measurements are correlated, with Pearson and Spearman coefficients of $r = 0.59$ and $\rho = 0.70$, respectively. To investigate the origin of this offset, we recalculated the qVAC-based black hole masses using the host-corrected continuum luminosity, $L_{5100,\mathrm{cor}} = \texttt{L5100}\,(1 - \texttt{FRAC_HOST_5100})$, as shown in Fig. C.2. Including the host contribution correction reduces the systematic difference between the two estimates, indicating that part of the discrepancy originates from differences in the continuum luminosity used in the virial mass estimator. The remaining scatter is primarily associated with differences in the measured broad Hβ line widths (Fig. C.3). In particular, the qVAC fitting procedure allows broad components up to approximately 15 000 km s^{-1} to account for possible redshift uncertainties. In some cases, this upper limit allows the fit to capture noise features as part of the broad component, resulting in artificially increased FWHM values and consequently higher virial black hole masses. Overall, the comparison demonstrates good statistical agreement between the two approaches, while highlighting systematic differences arising from continuum treatment and emission-line decomposition.

Fig. C.4 presents the comparison between the non-parametric velocity width W_{80} measured in this work and the values reported by qVAC. The two measurements are correlated, with Pearson and Spearman coefficients of $r = 0.42$ and $\rho = 0.75$, respectively. However, the comparison reveals a systematic difference for sources with strong outflow signatures. For the full sample, the median offset between the two measurements is 36 km s^{-1}, with a scatter of 479 km s^{-1} and an RMS deviation of 492 km s^{-1}. While the majority of sources show consistent measurements, the differences increase strongly towards high W_{80}. The fraction of objects for which our measurements exceed the qVAC values is 67%, indicating a systematic tendency towards larger velocity widths in our analysis. This difference becomes evident when separating the sample according to outflow strength. For sources without prominent outflows ($W_{80} < 800$ km s^{-1}), the median offset is only 16 km s^{-1}, with an RMS difference of 333 km s^{-1}. In contrast, moderate outflow sources ($800 \leq W_{80} < 1500$ km s^{-1}) show a median increase of 232 km s^{-1}, while extreme outflow sources ($W_{80} \geq 1500$ km s^{-1}) exhibit a much larger median difference of 1206 km s^{-1} and an RMS deviation of 1300 km s^{-1}. The increasing discrepancy at large velocity widths is caused by the limited ability of the qVAC fitting procedure to recover broad asymmetric outflow components. The qVAC measurements become increasingly incomplete above $W_{80} \approx 1400$ km s^{-1}, resulting in an underestimation of the strongest outflows. For example, the fraction of quasars classified as strong outflows decreases from 7.8% in our measurements to only 2.3% in the qVAC catalogue for $W_{80} > 1500$ km s^{-1}. This demonstrates that the qVAC catalogue is sufficient for identifying moderate kinematic signatures but does not reliably recover the extreme outflow population investigated in this work. Therefore, we use our measurements of W_{80} throughout the analysis.

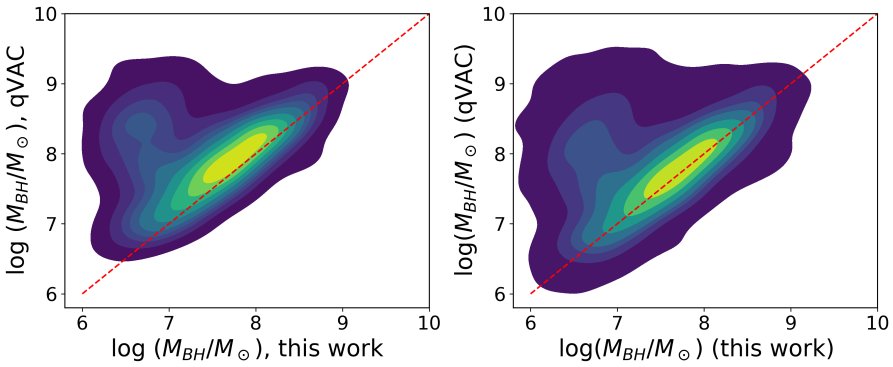


Fig. C.1: Comparison of the virial H_β black hole masses derived in this work, with results reported in the qVAC. Left: qVAC masses computed without host-corrected L_{5100}. Right: Comparison with masses based on host-corrected L_{5100}. The dashed red line indicates the 1:1 relation.

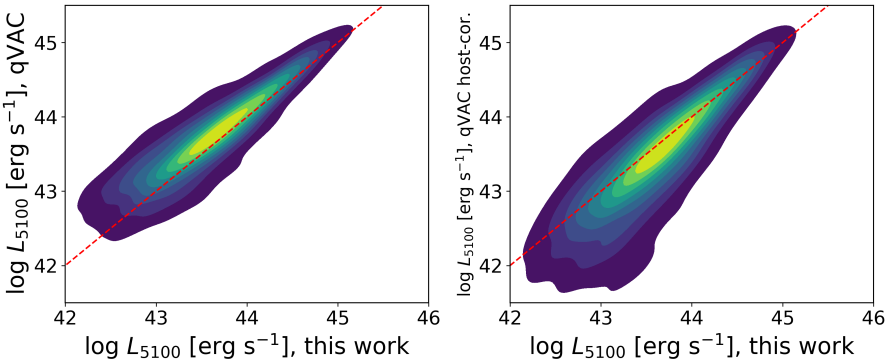


Fig. C.2: Comparison of the L_{5100} measurements from this work with values from the qVAC. Left: Comparison with the non–host-corrected qVAC luminosities. Right: Host-corrected values. The dashed red line indicates the 1:1 relation. The closer agreement with the non-host-corrected luminosities suggests that the host-galaxy contribution was not properly accounted for in the qVAC.

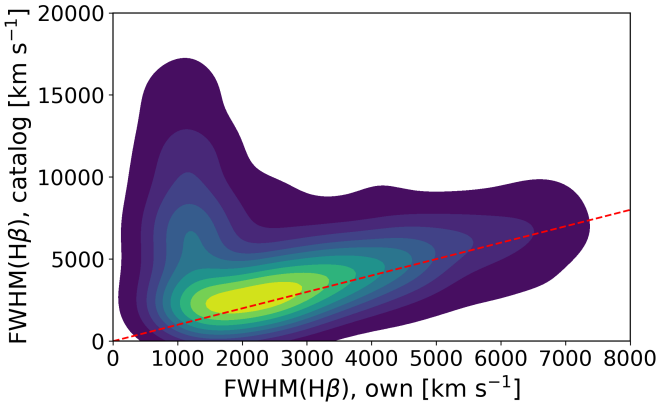


Fig. C.3: Comparison of the FWHM(Hβ) from this work with values from the qVAC. The dashed red line indicates the 1:1 relation.

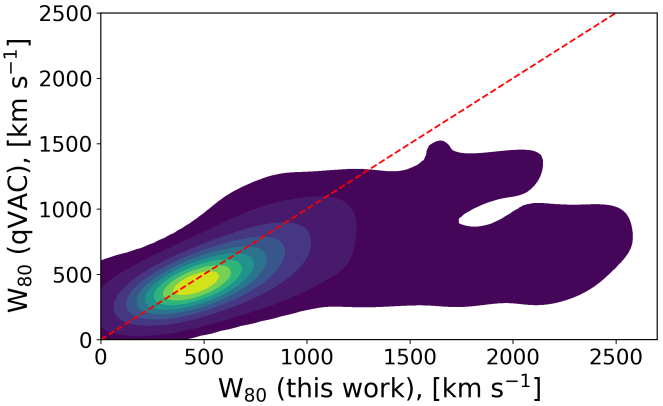


Fig. C.4: Comparison of the measured the W_{80} line width from this work with the values reported in the qVAC. The dashed red line indicates the 1:1 relation.

Appendix D: Example spectra

We present a few spectra as examples that are representative of extreme values for the model parameters. Fig. D.1 and D.2 display the quasar with the strongest outflow and the highest mass signatures, respectively. Most of the high outflow sources have a broad Hβ wing that hides the [O III] λ4959 Å emission line. As seen in these examples, the emission is mostly dominated by the AGN.
The quasar with the largest X-ray deficit (Fig. D.3) with $\Delta L_X = -1.44$ dex, $\log(L_X) \approx 10^{42}$ erg s^{-1} and $L_{6\mu m} \approx 10^{44}$ erg s^{-1}, has extremely high flux values, even compared with the other sources with MIR-normalised X-ray deficits. Additionally, its second [O III] component has an offset of (-425 ± 7) km s^{-1}, indicating a strong outflow.
Fig. D.4 shows the quasar with the smallest mass, but with a broad [O III] line ($W_{80} = 869$ km s^{-1}). Most of the low-mass sources have extremely high error bars for the mass. This result can be explained by the broad component of $H\beta$ being very weak or absent. In combination with the strong [O III] emission line, we can assume that the BLR is faint due to reddening or obscuration. Fig. D.5 and D.6 show the reddest quasar without and with outflow signatures, respectively. The first one is a bright source with narrow lines and an unreliable broad component for the SMBH mass estimation. The second source, meanwhile, shows generally broad features and a blueshifted [O III] component.

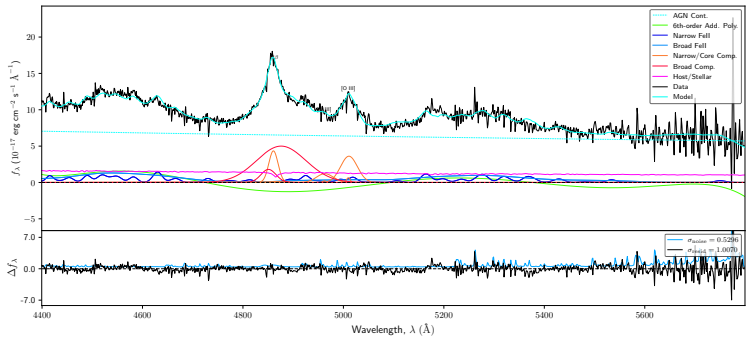


Fig. D.1: Spectrum of 100154-59940-27021598101868790 (J074852.89+085456.3) at $z = 0.782$, one of the strongest outflows in the sample, with $W_{80} = (2584 \pm 27)$ km s^{-1}. $\log(M_{BH}) = (8.97 \pm 0.07)\, M_\odot$, $\Delta L_X = -0.05$ dex, $(W1 - W2) = 1.14$

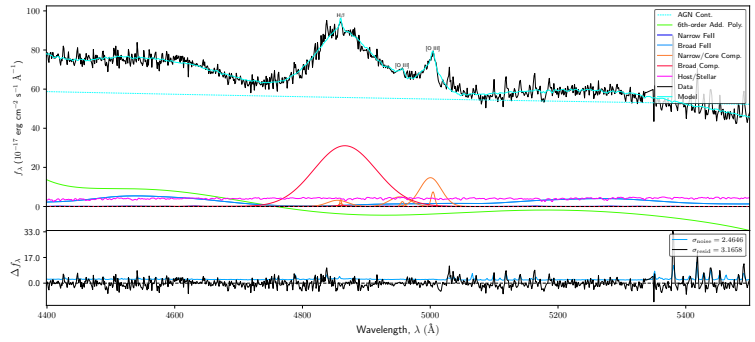


Fig. D.2: Spectrum of 101263-59949-27021598130954673 (J103413.86-020150.8) at $z = 0.743$, one of the massive quasars in the sample with $\log(M_{BH}) = (9.51 \pm 0.02)\, M_\odot$. $W_{80} = (2518 \pm 26)$ km s^{-1}, $\Delta L_X = -0.14$ dex, $(W1 - W2) = 1.17$

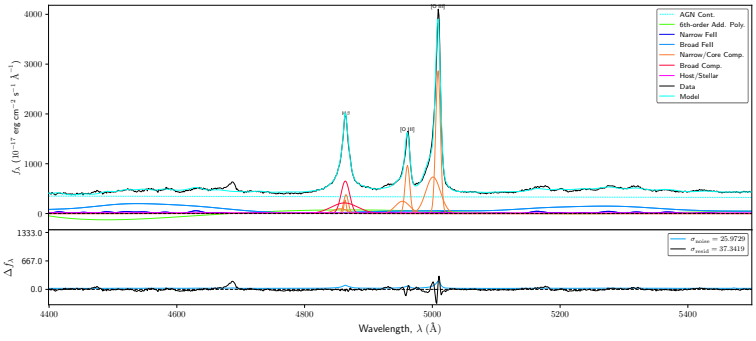


Fig. D.3: Spectrum of 101287-59679-27021598128436637 (J095219.10-013643.5) at $z = 0.0193$, the X-ray weakest source with $\Delta L_X = -1.44$ dex. $\log(M_{BH}) = (6.62 \pm 0.03)\, M_\odot$, $W_{80} = (1300 \pm 17)$ km s^{-1}, $(W1 - W2) = 1.05$.

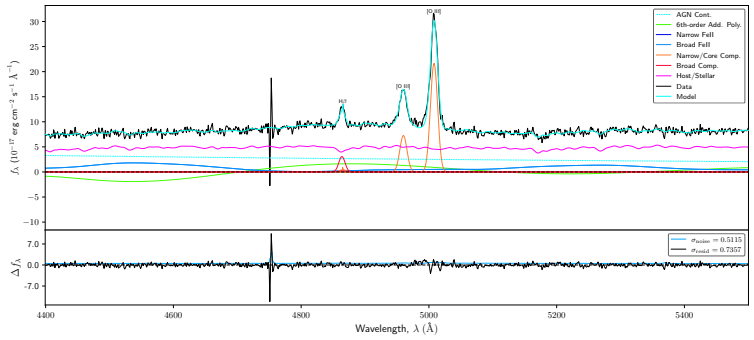


Fig. D.4: Spectrum of 100154-59940-27021598102059608 (J075439.90+101910.0) at $z = 0.173$, quasar with a weak $H\beta$ signal, but still outflow signatures. $\log(M_{\rm BH}) = (6.12 \pm 0.28)\,M_\odot$. $W_{80} = (869 \pm 1)\,{\rm km\,s^{-1}}$, $\Delta L_{\rm X} = 0.14$ dex, $(W1 - W2) = 0.84$.

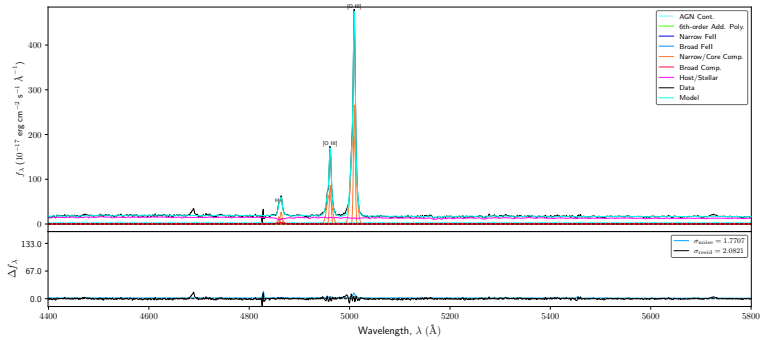


Fig. D.5: Spectrum of 103959-59964-27021598053510246 at $z = 0.155$, the reddest source without an outflow $(W1 - W2) = 1.62$, $\log(M_{\rm BH}) = (6.6 \pm 1.5)\,M_\odot$, $\Delta L_{\rm X} = -1.21$ dex, $W_{80} = (657 \pm 6)\,{\rm km\,s^{-1}}$.

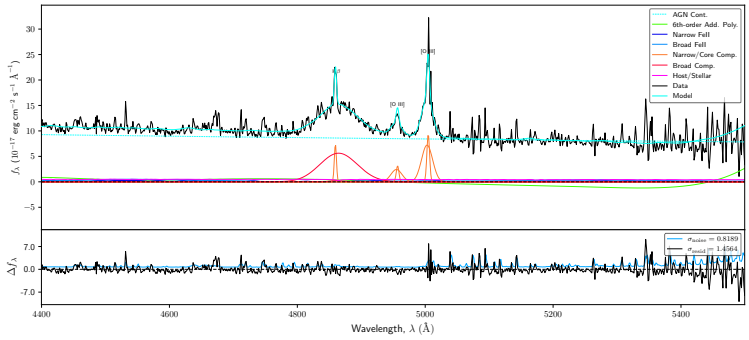


Fig. D.6: Spectrum of 104363-59935-27021598101916100 (J075759.36+065534.9) at $z = 0.155$. It is the reddest source with $(W1 - W2) = 1.43$ but with outflow signatures and strong blue wing ($v_{off} = -321 \pm 4\,{\rm km\,s^{-1}}$). $\log(M_{\rm BH}) = (8.72 \pm 0.03)\,M_\odot$, $\Delta L_{\rm X} = 0.5$ dex, and $W_{80} = (1188 \pm 30)\,{\rm km\,s^{-1}}$.